ASME Journal of Engineering for Gas Turbines and Power
Online journal at:
https://asmedigitalcollection.asme.org/gasturbinespower

Ceramic and Metal Additive Manufacturing of Monolithic Rotors From SiAlON and Inconel and Comparison of Aerodynamic Performance for 300W Scale Microturbines

Lukas Badum
Aerospace Engineering Department,
Turbomachinery and Heat Transfer Laboratory,
Technion–Israel Institute of Technology,
Haifa 3200003, Israel
e-mail: lukas@campus.technion.ac.il

Thomas Prochaska
Lithoz GmbH,
Wien 1060, Austria
e-mail: tprochaska@lithoz.com

Martin Schwentenwein
Lithoz GmbH,
Wien 1060, Austria
e-mail: mschwentenwein@lithoz.com

Beni Cukurel[1]
Aerospace Engineering Department,
Turbomachinery and Heat Transfer Laboratory,
Technion, Israel Institute of Technology,
Haifa 3200003, Israel
e-mail: beni@cukurel.org

The gas turbine industry is continuously developing and testing new materials and manufacturing methods to improve the performance and durability of hot section components, which are subjected to extreme conditions. SiAlON and Inconel 718 are especially desirable for turbomachinery applications due to their high strength and high-temperature capabilities. To demonstrate the viability of additive manufacturing for small-scale turbomachinery for 300W scale microturbines, a monolithic rotor with a design speed of 450,000 RPM containing radial turbine and compressor was developed considering additive manufacturing constraints. The geometry was manufactured from SiAlON and Inconel 718 using lithographic ceramic manufacturing and selective laser melting, respectively. The additive manufacturing and thermal process parameters as well as material characterization are described in detail. Surface and computerized tomography scans were conducted for both rotors. While the metallic rotor showed undesirable printing artifacts and a large number of defects, the ceramic part achieved a level of relative precision and surface quality similar to large-scale production via casting. To compare turbomachinery performance, an aerodynamic test facility was developed allowing to measure pressure ratios and efficiency of small compressors. The rotors were tested in engine-realistic speeds, achieving a compressor rotor pressure ratio of 2.2. The ceramic part showed superior efficiency and pressure ratio compared to the Inconel rotor. This can be explained by lower profile and incidence losses due to a higher fidelity physical representation of the model geometry and better surface finish. [DOI: 10.1115/1.4063421]

Keywords: additive manufacturing, lithographic ceramic manufacturing, selective laser melting, powder-bed-fusion, ceramic materials, micro turbomachinery, micro gas turbine

1 Introduction

The market for small unmanned aerial vehicles is experiencing significant growth, leading to an increasing demand for portable power supply systems with electric outputs below 1 kW [1]. Microturbines are small-scale heat engines that consist of a generator, radial compressor, combustion chamber, and radial turbine, which work together to convert chemical energy into electrical energy. At 1 kW power output, these systems have rotors with tip diameters below 30 mm and rotational speeds above 300,000 RPM, making them compact and efficient power supply systems. Microcompressor and turbine performance in these scales are deteriorated by low Reynolds numbers, high relative surface roughness, and large relative tip clearance [2,3]. To achieve acceptable part cost and aerodynamic efficiency, complex three-dimensional (3D) blade geometries are necessary, requiring advanced manufacturing technology.

Additive manufacturing (AM) methods are an excellent alternative for achieving cost-effective production of complex small-scale parts as, in contrast to conventional manufacturing, multiple components can be printed in parallel on a single machine, resulting in a drastic cost reduction. Selective laser melting (SLM) is a powder-bed-fusion process whereby a high-density-focused laser beam scans a powder bed, and those solidified layers are stacked upon each other to build a fully functional three-dimensional metallic part. In large-scale gas turbines, SLM is facilitated to manufacture stationary parts like vane segments and fuel nozzles due to superior geometric flexibility and durability [4]. Moreover, SLM has been used to manufacture small-scale radial turbines with internal air cooling channels [5]. For these applications, Inconel 718

[1]Corresponding author.

Manuscript received August 6, 2023; final manuscript received August 20, 2023; published online October 25, 2023. Editor: Jerzy T. Sawicki.

alloy is applied due to its creep and oxidation resistance and high yield strength at elevated temperatures. It has been shown that Inconel 718 components manufactured with SLM technology exhibit similar or better properties than conventionally manufactured parts [6]. Beside nickel alloys, technical ceramics have been suggested as material for hot-section turbine components due to their excellent high-temperature capabilities, low density, and high strength [1]. Multiple feasibility studies and experimental tests of ceramic gas turbine components have shown that silicon nitride based SiAlON ceramics are most favorable for this application due to their superior hardness and high-temperature properties, which may be comparable to or even better than those of pure silicon nitride [7–10]. Furthermore, dense SiAlON parts can be fabricated in low-pressure sintering atmosphere [11]. Previously, Kang et al. investigated indirect AM of monolithic SiAlON rotors by gel casting rapid prototyping [12–14]. However, the technology requires CNC machining of multiple fugitive wax molds for each rotor and is therefore not competitive with conventional methods. A breakthrough for additive manufacturing of SiAlON components has only recently been achieved by lithographic ceramic manufacturing (LCM) technology, particularly suitable for centimeter-scale parts due to high print resolution and low minimum feature size.

2 Motivation and Objective

Additive manufacturing of monolithic microturbine rotors allows for the creation of cost-effective, highly complex, and precise geometries that may be difficult or impossible to achieve through traditional manufacturing methods. Additionally, the use of SiAlON ceramic material allows for enhancement of achievable turbine inlet temperature, pressure ratio, and cycle efficiency. The objective of this work is to evaluate and compare the aerodynamic performance of monolithic microgas turbine rotors manufactured with SLM and LCM technologies. To this end, a new rotor architecture is considered to incorporate all components on a single part including an internal cooling cavity contrasting conventional manufacturing which requires separate production of compressor, turbine, and shaft [4,6,20,21]. The monolithic rotor architecture results in fully functional rotors printed in a single uninterrupted process. Manufacturing constraints and their effect on turbomachinery design are discussed and the rotor geometry development is described. Since LCM has not been reported previously for turbomachinery components, process parameters and adaptations required are reported in detail. Subsequently, manufacturing quality of SLM and LCM processes are compared. Finally, successful high-speed tests up to 450,000 RPM are conducted, comparing the aerodynamic performance of metal and ceramic rotors. To the best knowledge of the authors, this is the first effort to examine and demonstrate monolithic rotors under relevant turbine tip speeds manufactured with LCM and SLM.

3 Methodology

3.1 Microturbine Layout. The microturbine combines an electric generator and heat engine in a single device. It uses a Brayton cycle, which consists of a compressor, combustion chamber, and turbine, to convert chemical energy into shaft power. Unlike larger engines, which typically use axial multistage components, the microturbine employs single-stage radial turbomachinery to achieve the required pressure ratios. This allows it to operate according to the same thermodynamic principles but on a smaller scale. In the microgenerator, the excess power generated by the heat engine is converted to electric power which can be transferred to a consumer. As shown in Fig. 1, the electric generator is located at the cold end of the assembly, upstream of the compressor. This arrangement thermally decouples the heat engine and electric machine by using an overhung rotor geometry. Furthermore, the bearings can be placed on the cold side of the engine, thus easing up thermal loads and increasing bearing lifetime.

The rotor of the microturbine operates under extreme conditions due to the high combustion temperatures and centrifugal forces,

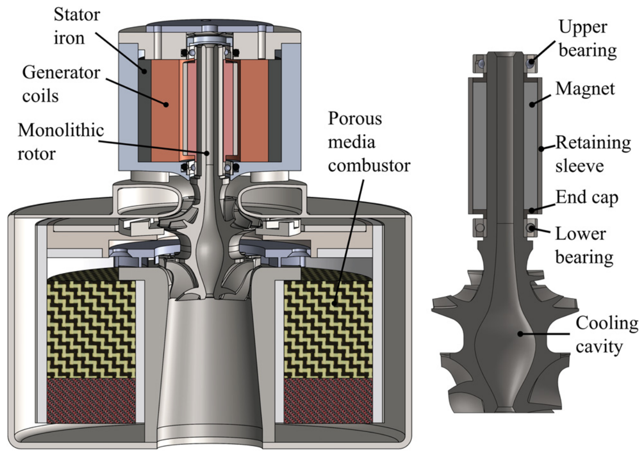

Fig. 1 Microturbine topology and rotor layout

requiring the use of materials with high capabilities and an integrated design to meet these demands. The upper rotor shaft on the cold side of the microturbine contains two angular contact bearings and a generator magnet. For the generator topology, a 2-pole, 3-phase permanent magnet synchronous machine (PMSM) with slotless stator design is selected. The magnet dimensions are designed based on literature for similar high-speed machines [15–17] as well as rotordynamic analysis, making sure to sustain an acceptable threshold between operating frequency and first critical bending speed. A Sm2Co17 magnet with axial length of 15 mm and outer radius of 3.5 mm is selected. To maintain required stress limits, a titanium retaining sleeve with 0.7 mm radial thickness is pressed on the magnet. In the considered gas turbine topology, the rotor contains the turbomachinery components and is equipped with a patented passive cooling system consisting of an internal cavity, potentially enhanced by internal vanes [18]. Main rotor parameters are summarized in Table 1.

3.2 Rotor Geometry. While LCM and SLM allow enhanced geometric flexibility as compared to conventional manufacturing, the layer-by-layer printing process also imposes geometric constraints [1]. To enable overhung geometries, it is common practice in AM to use support structures on the build plate or the part itself, which are removed after the print. However, this approach results in artifacts, high surface roughness, and potential damage. The impact on functionality is even more important for small scales, as the relative size of these defects increases. To bypass these shortcomings, a monolithic microturbine rotor is designed to comply with support-free manufacturing. As depicted in Fig. 2, the rotor is printed from turbine toward compressor side, creating the advantage that the aerodynamically more sensitive compressor is manufactured in nonoverhung condition. Moreover, contour slopes above 55 deg are avoided, being the maximum support-free angle that can typically be achieved without part deformation [19].

The impact of this constraint on turbomachinery design and performance should be considered. Since compressor leading and turbine trailing edge are in the axial section of the flow path, the blade angles in this region must follow the support-free design limitation. The compressor leading edge blade angle determines the design point inlet velocity triangle. Since rotor losses are generated

Table 1 Rotor geometry specifications

Shaft diameter	4 mm
Bearing width	2 mm
Bearing outer diameter	7 mm
Magnet length	15 mm
Magnet diameter	7 mm
Sleeve thickness	0.7 mm

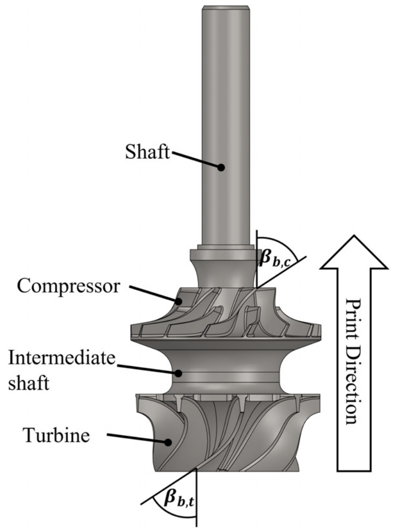

Fig. 2 Rotor geometry with compressor and turbine shroud blade limits and print direction

depending on relative frame flow conditions, a good compressor design should aim for minimum relative velocity at inlet. Rusch and Casey derived the optimum compressor inlet blade angle independent of geometric features and pressure ratio [20]. To this end, they introduced a normalized mass flow function indicating the relative inlet Mach number as a function of the inlet shroud blade angle. If the normalized mass flow function is at its peak, minimum shroud velocities and thus losses occur in the rotor for given design conditions. Figure 3 adapts the results published in Ref. [20] with indication of the maximum angle achievable using support-free printing. The optimum shroud blade angle ranges between 55 deg at low to 65 deg at high flow coefficients, exceeding the manufacturing constraint. Using support-free printing technique therefore introduces an efficiency penalty caused either by incidence if the optimum flow angle is maintained, or by enhanced relative velocity levels if the flow angle is equal to the blade angle.

Figure 3 shows that this effect is aggravated for high relative shroud Mach numbers, which generally occur at higher flow coefficient compressor designs. The proposed design method is therefore expected to be most suitable for low flow coefficient compressors. Since radial turbines are usually not followed by a vaned diffuser, the circumferential velocity energy cannot be regained. Therefore, the exit blade angle is often chosen to achieve

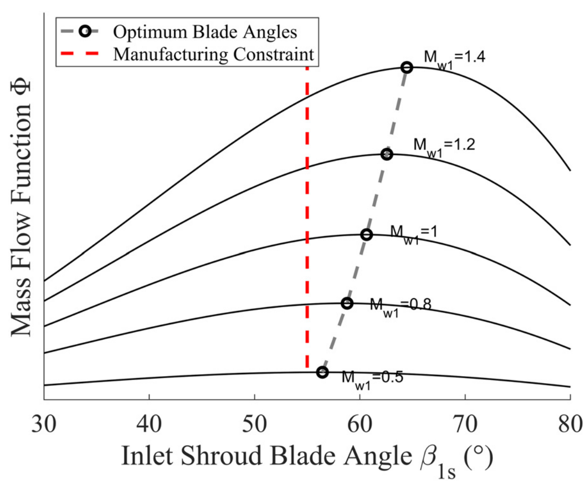

Fig. 3 Optimum compressor leading edge blade angle, reconstructed from [20]

axial flow at design point. However, this strategy can result in blade angles well above 60 deg, ruling out support-free additive manufacturing. The design approach of the radial turbine should therefore follow a similar consideration as discussed for the compressor by minimizing the outlet relative velocity as suggested by Whitfield [21], who concluded that optimum rotor total to total efficiency is achieved for outlet blade angles around 60 deg. By constraining the turbine outlet blade angle to 55 deg, additional exit loss is accepted while accomplishing a support-free blade geometry. Compared to the compressor, the efficiency penalty paid is low as the upstream flow field is not affected. For the turbine trailing edge, a cutoff design is selected to create a flat surface at the lower end of the rotor which can be attached to the printer build plate. Since the turbine extends radially, part of the blade and hub geometry is parallel to the build plate exceeding the required 55 deg slope. However, tests have shown that a short overhung can be tolerated without significant part deformation. In addition to the maximum overhung angle, the minimum turbomachinery blade thickness is limited. During iterative manufacturing of different rotor geometries, it was found that blades should be at least 300 μm thick to avoid manufacturing artifacts and crack formation in the green body. For thinner blades, cracks were observed during debinding which may be attributed to the large volume loss in this process stage, see Refs. [22] and [23]. In this case, the rotors cannot be used as blade features are missing. Using the discussed turbomachinery design approach, compressor and turbine geometries are determined using ANSYS VISTA CCD and ANSYS VISTA RTD, respectively, main design parameters are given in Table 2.

Based on a previously published cycle analysis for a 300W microturbine engine [1], the microcompressor is designed to operate at a maximum pressure ratio of 2.2 with tip speed up to 380 m/s corresponding to tip Mach number close to unity. The design rotor speed is set to 450,000 RPM to facilitate ball-bearing technology. Simulations of the rotor's conjugate heat transfer indicate that, at the design turbine inlet temperature of 930 °C, the maximum turbine blade root temperature falls between 680 °C and 700 °C. Figure 4 shows the results of a stress analysis of the radial turbine side, revealing that Inconel 718 rotor stresses are about 2.5 times higher than those of the SiAlON rotor, which corresponds to the density ratio of the materials. The highest stresses recorded at the turbine blade root were 520 MPa for Inconel 718 and 208 MPa for SiAlON. It is worth noting that SiAlON has a higher temperature limit and, as a result, the turbine inlet temperature could potentially be raised by up to 300 °C, leading to a substantial improvement in cycle efficiency.

3.3 Additive Manufacturing of SiAlON Rotors. LCM is a direct AM method for producing highly dense ceramic components with material properties comparable to conventional manufacturing methods. As described in Refs. [22] and [24], the process is based on layer-wise solidification of a photosensitive suspension with 40% SiAlON volume share ("LithaNit 780"). The slurry is applied on the vat with a wiper and the building platform is lowered above the vat, generating a gap typically between 10 μm and 100 μm depending on required accuracy. A light mask is projected on the translucent vat according to the two-dimensional layer geometry. The photosensitive binder solidifies, forming a thin extrusion on the building platform or the previous part layer. This way, green bodies containing SiAlON particles and binder are shaped. The material parameters of the SiAlON suspension are tailored to the manufacturing process considering various constraints. First, the suspension must be highly viscous for thin film application on the vat. The viscosity also influences the waiting time before light exposure and thus printing speed. Furthermore, the material curing depth must be at least three times the desired layer height to avoid cracking of the green body during thermal postprocessing [22,23]. The curing depth is a function of exposure light intensity, waiting time, and optical properties of the suspension. Besides this, good adhesion to the building platform is required for the initial layer to keep the part in place; at the same time, new layers must not stick to the translucent

Table 2: Turbomachinery design parameters

Parameter	Compressor	Turbine
Inlet blade height	2 mm	1.3 mm
Outlet blade height	1.1 mm	3.8 mm
Tip radius	8 mm	7.9 mm
Inlet shroud blade angle/outlet shroud blade angle	56.3 deg	57.4 deg
Backsweep/outlet blade angle	45 deg	60 deg
Blade thickness	0.26–0.38 mm	0.5–0.6 mm
Number of blades	7 + 7	9
Number of stator blades	Vaneless	15

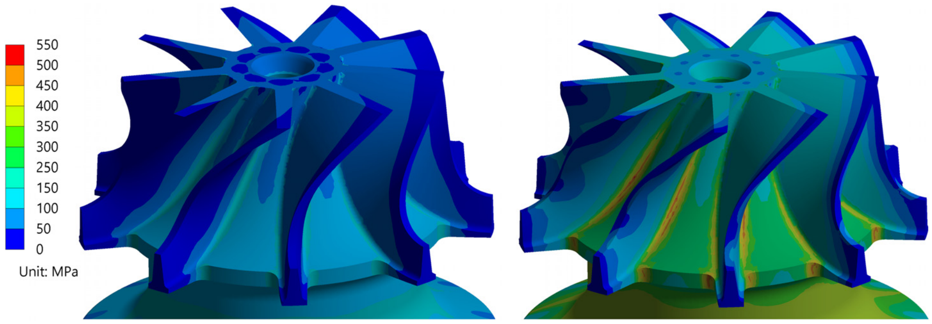

Fig. 4 Turbine stress analysis comparison for SiAlON (left) and Inconel 718 rotor (right)

Fig. 5 Rotor LCM printing process

vat, which would cause printing failure by green body detachment or break. The main difficulties in printing SiAlON slurries result from light scattering and high levels of UV absorption. Thus, the curing depth is reduced compared to Alumina or Zirconia slurries, and the risk of crack formation during debinding is increased. Furthermore, the relatively low viscosity favors vat adhesion. This is particularly challenging for the proposed monolithic rotor geometry. The rotors were attached to the building platform at the cut-back turbine blades as depicted in Fig. 5. Best print results were obtained with process parameters specified in Table 3.

During the first test prints, build plate detachment was repeatedly observed when the compressor backplate was reached. Due to the large surface area at this location, adhesive forces of the vat exceeded the adhesive forces on the build-plate. This effect was avoided by increasing the cavity's internal dimensions compared to the initial geometry as depicted in Fig. 6. As the first layer structure can be damaged during removal from the build plate, an axial extension of the turbine end surface was created which was removed by grinding after the sintering process. Once the green body turbine rotor was produced and cleaned from residual resin, the organic binder was removed in the debinding process by long-term exposure to temperatures up to 600 °C in an air furnace (HTCT 08/16, Nabertherm, Lilienthal, Germany) with a temperature profile according to Fig. 7.

In a previous study [22], the weight loss of samples during debinding was determined using thermogravimetric analysis. As depicted in Fig. 7, majority of weight loss occurs at temperatures below 400 °C. To remove the binder from the furnace, air ventilation was ensured, and the binder residuals were collected in a storage tank. The white bodies were densified in a two-step sintering oven (KCE HPW 150/200-2200-100 LA) starting in vacuum up to holding temperature of 600 °C and continuing in nitrogen atmosphere with ramped temperatures up to 1750 °C according to Fig. 8.

3.4 Additive Manufacturing of Inconel 718 Rotors. To compare manufacturing quality and aerodynamic performance, the presented rotor geometry was manufactured from Inconel 718 by a subcontractor on a SLM Printer (SLM 125, SLM Solutions, Lübeck, Germany) with 30 μm layer height and volumetric energy

Table 3: LithaNit 780 printing process properties

Layer thickness	Wavelength	Light intensity	Energy dose
20 μm	460 nm	47.1 W cm^{-2}	450 mJ cm^{-2}

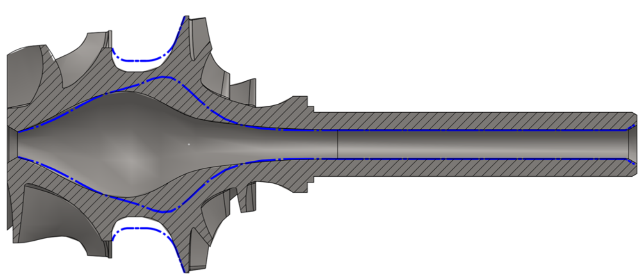

Fig. 6 Inconel 718 rotor (full) and SiNi rotor contour adjustment (dash-dotted)

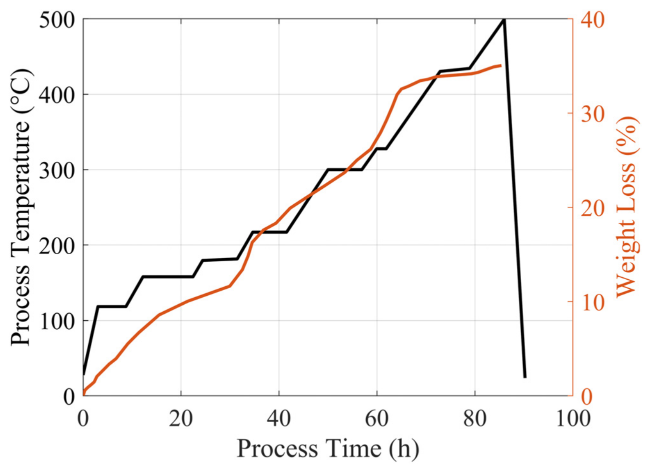

Fig. 7 Drying and debinding process with associated weight loss and highlighted region for spiked storage

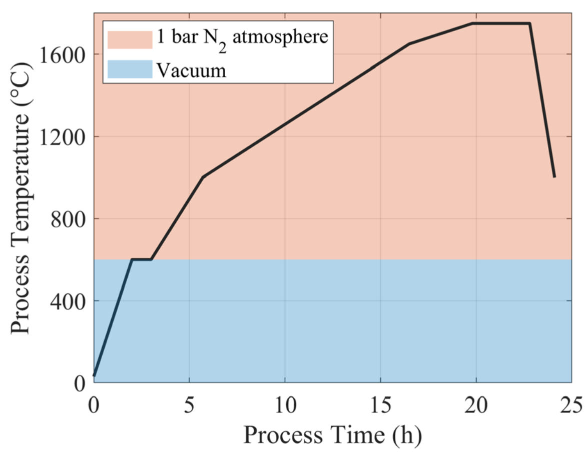

Fig. 8 Two-step sintering profile for LithaNit 780

density $\mathrm{VED} = 61.2\,\mathrm{J/mm^3}$ calculated from laser power P, scanning speed V, hatching distance h and layer height t [25]

$$\mathrm{VED} = \frac{P}{Vht} \tag{1}$$

Further details on SLM manufacturing are not elaborated here as the process is well established. An optimization study of printing parameters can be found in Ref. [25] while material properties of Inconel 718 manufactured with SLM are described in Ref. [6]. To improve surface quality of Inconel 718 rotors, sandblasting was applied to all surfaces.

3.5 Rotor Assembly and Balancing. The raw rotor shaft is manufactured with an oversize of 0.5 mm and center holes are provided on the axial end surfaces. The components are ground between centers on the bearing shaft to a tolerance field of 3 μm. Subsequently, the rotors are assembled by pressing angular contact bearings, magnet, and titanium sleeve on the shaft resulting in functional prototypes as depicted in Fig. 9.

To ensure proper operation, dynamic balancing to grade G6.3 according to ISO 21940-11 [26] is conducted. To this end, the upper half of the test facility containing the microrotors is mounted on a high-precision balancing machine (HD-1, BalanceMaster, Inc., Concord, VA). Figure 10 depicts the balancing assembly. The rotor is driven by a supply air nozzle. Different balancing speeds have been tested, and the best results were achieved at 15,000 RPM. The first balancing plane lies on the titanium sleeve between the bearings

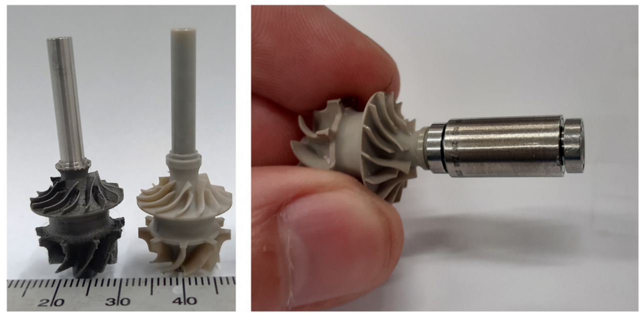

Fig. 9 SLM produced Inconel 718 and LCM produced SiAlON rotors after grinding (left) and bearing/magnet assembly (right)

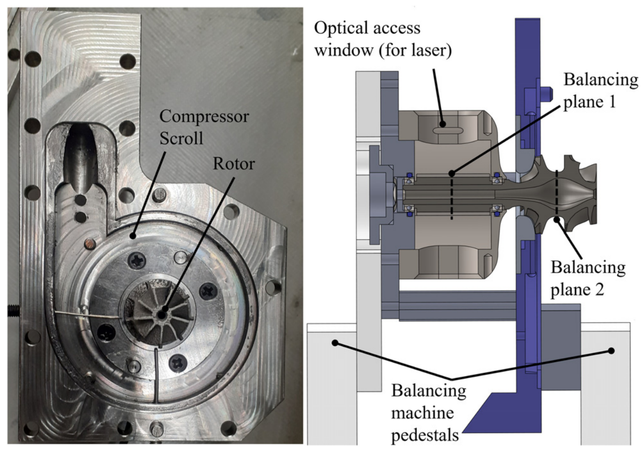

Fig. 10 Rotor in casing assembly (left), balancing configuration with planes to remove material (right)

and can be accessed from the top through a sight window. The second balancing plane is located on the overhung rotor side between turbine and compressor. Material is removed according to the calculated imbalance using an engraving laser located above the balancing assembly. This approach ensures a repeatable result, and the assembly can be mounted on the aerodynamic test rig after balancing without removing the rotor from its casing. Balancing can only be achieved effectively if the rotor runout is below 150 μm, as otherwise large material removal would be required, potentially compromising the structural integrity of the rotor and sleeve.

3.6 Rotor Test Facility. A test facility was developed for commissioning of the additively manufactured rotors in realistic tip speeds and for the evaluation of the compressor's aerodynamic performance. Two separate flow paths are established for compressor and turbine. The turbine inlet airflow and pressure are set by a flow controller such that the desired design speed is achieved for each operating point of the compressor. To reduce heat transfer to and from the compressor, the turbine inlet temperature (T_{3t}) is controlled by an electric heater to the average measured flow temperature between compressor inlet (T_{1t}) and outlet (T_{2t})

$$T_{3t} = (T_{1t} + T_{2t})/2 \tag{2}$$

The heated air then passes the guide vanes and expands in the radial turbine, leaving the test rig axially. On the compressor side, ambient air is sucked in and compressed by the impeller and the vaneless diffuser. The exhaust pressure of the compressor is throttled by a valve downstream. The gas paths are summarized in Fig. 11.

The physical assembly consists of a steel bearing housing, a compressor section, an intermediate section, and a turbine section, Fig. 12. The sections are centered by centering pins and sealed by

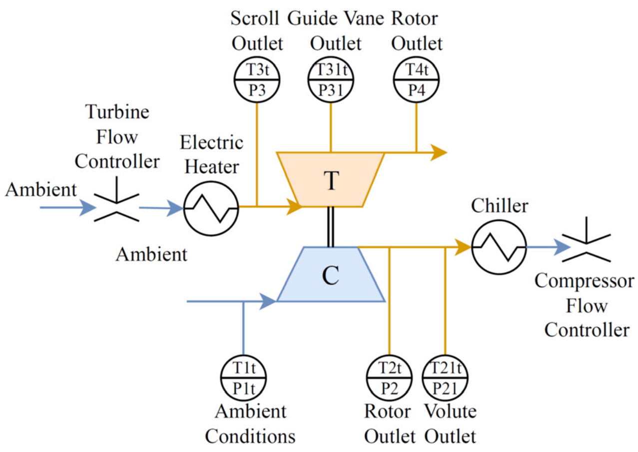

Fig. 11 Rotor test facility flowchart

laser-cut graphite seals. To investigate various compressor and turbine geometries, the casing contours can be exchanged in both sections, allowing a tip height variation up to 2 mm with compressor and turbine radii up to 10 mm. For the tests conducted, two PTFE shroud inserts were machined to minimize heat flux to and from the compressor and turbine flow path, thus minimizing diabatic effects.

Furthermore, the intermediate shaft seal, which separates turbine and compressor flow path, can be exchanged to allow different intermediate shaft diameters. The seal consists of two laser-cut graphite half-rings sized to initially scratch the intermediate shaft separating compressor and rotor. During startup of the rotor, the seal was then rubbed in against the intermediate shaft, creating a narrow gap and thus ensuring minimum leakage flow between turbine and compressor. The axial tip clearance of the compressor was adjusted by modifying the length of the axial spacers between bearing casing and compressor volute and measuring the resulting gap with a feeler gauge. For the tests, it was set to 150 μm. The compressor vaneless diffuser is selected according to best practice guidelines in relation to the prototype compressor radius, see Casey [27]. Reynolds averaged Navier Stokes (RANS) simulations were used to design the turbine volute with a uniform outlet flow angle. The nozzle guide vanes were designed according to the design flow angle of the turbine at engine inlet conditions at 1200 K inlet temperature and 2.2 bar.

To evaluate the aerodynamic performance of the compressor, total temperatures and total and static pressures must be measured at the impeller inlet and outlet, as indicated in Fig. 12. The inlet total pressure (P_{1t}) was determined from ambient pressure measurement.

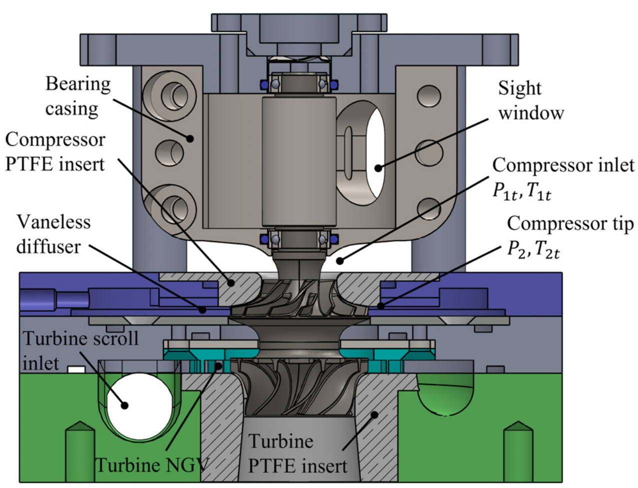

Fig. 12 Rotor test facility cross section

The inlet total temperature (T_{1t}) was measured using a 0.5 mm diameter K-type thermocouple placed in the flow path directly upstream of the compressor inlet, which takes into account the heating of the incoming compressor air by the adjacent casing walls. The static pressure (P_2) and total temperature (T_{2t}) at the compressor tip were measured using static pressure taps and T-type thermocouples on three circumferential measurement stations on the PTFE shroud insert, as depicted in Fig. 13. The resulting values were determined from the average measurements of the three stations. On the turbine side, the inlet temperature T_{3t} upstream of the nozzle guide vanes was calculated by averaging temperature measurements of three K-type thermocouples circumferentially distributed in the turbine scroll. The rotor speed was measured by a laser tachometer (LT-880, Terahertz Technologies, Oriskany, NY). Control and data logging of the test facility were performed via in-house LABVIEW code.

To accurately evaluate and compare the compressor performance between Inconel 718 and SiAlON rotors from experimental data, an uncertainty analysis was conducted for the compressor total to total pressure ratio and total to total polytropic efficiency. The total pressure at the rotor exit P_{2t} can be calculated from the measured static pressure P_2, heat ratio γ, and Mach number M_2

$$P_{2t} = P_2\left(1 + \frac{\gamma - 1}{2}M_2^2\right)^{\frac{\gamma}{\gamma-1}} \tag{3}$$

The calculated tip flow Mach number results from mass flowrate $\dot{m}_c$, static pressure P_2, geometric tip area A_2, flow blockage B_2, and circumferential velocity component c_u

$$M_2 = \frac{\sqrt{\left(\frac{\dot{m}_c}{P_2/(RT_2)A_2(1-B_2)}\right)^2 + c_{u2}^2}}{\sqrt{\gamma R T_2}} \tag{4}$$

The static rotor tip temperature T_2 is determined from the measured total temperature T_{2t} using a baseline recovery factor of $F_{\rm rcv} = 0.815$ as suggested by Fernelius [28]

$$T_2 = T_{2t}\left(1 + F_{rcv}\frac{\gamma - 1}{2}M_2^2\right)^{-1} \tag{5}$$

The rotor polytropic total-to-total efficiency is calculated as follows:

$$\eta_{\rm ptt} = \frac{\gamma - 1}{\gamma}\ln\left(\frac{P_{2t}}{P_{1t}}\right)/\ln\left(\frac{T_{2t}}{T_{1t}}\right) \tag{6}$$

With the given equations, the total pressure uncertainty can be derived as

$$\Delta P_{2t} = \sqrt{\left(\frac{\partial P_{2t}}{\partial P_2}\Delta P_2\right)^2 + \left(\frac{\partial P_{2t}}{\partial M_2}\Delta M_2\right)^2} \tag{7}$$

According to ISO 5168:2005, if an uncertainty contribution is less than 20% of the largest contribution, it can be considered

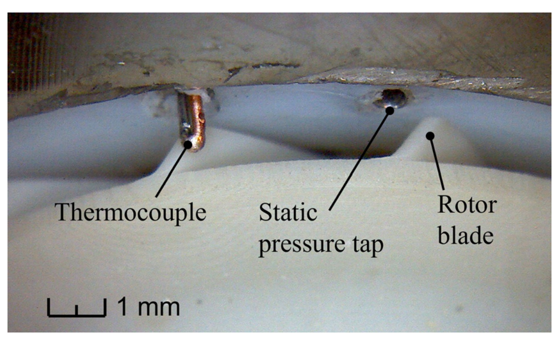

Fig. 13 Rotor tip instrumentation

insignificant and disregarded [29,30]. As mass flowrate $\dot{m}_c$ is measured with high accuracy and the circumferential velocity c_{u2} is mainly a function of tangential rotor speed, the Mach number error is calculated by

$$\Delta M = \sqrt{\left(\frac{\partial M}{\partial P_2}\Delta P_2\right)^2 + \left(\frac{\partial M}{\partial B_2}\Delta B_2\right)^2 + \left(\frac{\partial M}{\partial T_2}\Delta T_2\right)^2} \tag{8}$$

Using CFD simulations, it was found that the flow blockage at the compressor tip B_2 is high as the selected De-Haller number results in flow separation in rotor flow passage. The flow blockage was modeled using a blockage model by Aungier [31] to fit CFD data, assuming a model accuracy of $\Delta B_2 = 0.1$. For a given Mach number, the static temperature uncertainty is then

$$\Delta T_2 = \sqrt{\left(\frac{\partial T_2}{\partial T_{2t}}\Delta \mathrm{T}_{2\mathrm{t}}\right)^2 + \left(\frac{\partial T_2}{\partial F_{\mathrm{rcv}}}\Delta F_{\mathrm{rcv}}\right)^2} \tag{9}$$

As the total inlet pressure is determined with high accuracy from the ambient conditions, the uncertainty is then given by

$$\Delta \eta_{\mathrm{ptt}} = \sqrt{\left(\frac{\partial \eta_{\mathrm{ptt}}}{\partial P_{2t}}\Delta \mathrm{P}_{2\mathrm{t}}\right)^2 + \left(\frac{\partial \eta_{\mathrm{ptt}}}{\partial T_{1t}}\Delta T_{1t}\right)^2 + \left(\frac{\partial \eta_{\mathrm{ptt}}}{\partial T_{2t}}\Delta T_{2t}\right)^2} \tag{10}$$

Table 4 summarizes errors and uncertainties of each parameter. Acceptable uncertainties are expected for the total pressure measurement, while efficiency uncertainty can reach high values. This is the case for low total pressure ratios and mass flow rate. However, as the aerodynamic tests are conducted under equal conditions, it is expected that efficiency trends are captured correctly. Acceptable efficiency uncertainty is reached for high flow rates and pressure ratios.

3.7 Numeric Simulations. To compare measured performance data of the printed microrotors to numeric predictions, high-fidelity RANS simulations of the compressor stage were conducted in ANSYS CFX using the standard shear-stress transport k-omega turbulence model which is commonly suggested for turbomachinery [32,33]. The simulation involved a single rotating domain that included the radial inlet section, rotor, and vaneless diffuser. Consequently, there was no need for a rotor–stator interface. The tip clearance between compressor rotor and shroud was adjusted to 0.15 mm corresponding to the value of the experimental setup. As boundary conditions, the experimentally measured inlet total temperature and pressure as well as the outlet mass flow and rotational speed were prescribed for each design point. All walls were treated as smooth and adiabatic. Thus, the computational fluid dynamic (CFD) simulation presents a baseline comparison case excluding aerodynamic performance reduction caused by surface roughness, diabatic effects, and printing artifacts. A study on mesh refinement revealed that the CFD predictions of pressure ratio and efficiency reached a satisfactory level of convergence at around 470k elements. This mesh size was then chosen as the design mesh. The simulations were conducted until convergence of mass, momentum, and rotor efficiency was achieved. All thermodynamic quantities were evaluated by area-averaged values in two subsequent radial planes directly downstream of the rotor. This approach is consistent with the time and space averaged values obtained by sensor data measurement.

Table 4 Measurement and modeling accuracy

Measured parameter	Origin	Calculated measurement accuracy
T_{1t}	Measured	±3.5 °C
P_2	Measured	±1500 Pa
T_{2t}	Measured	±3 °C
F_{rcv}	Calculated	0.1
B_2	Calculated	0.1
Calculated parameter	**Relative uncertainty**	**Absolute uncertainty**
π_{ptt}	±1.2% to ±3%	±0.02 to ±0.06
η_{ptt}	±4 to ±12%	±2.8 to ±10%

4 Results and Discussion

4.1 Manufacturing Quality Assessment. The dimensional accuracy of compressor and turbine blade surfaces influences the aerodynamic performance of the components. Discrepancies between design and manufacturing can result in distortion of velocity triangles and flow profiles within the passage. To ensure reasonable flow guidance at small scales, it is therefore necessary to also reduce the tolerance limits of the blade structure. The dimensional deviations from additive manufacturing are therefore normalized by the compressor tip radius and compared to cast turbomachinery components in the automotive industry. Typical car turbocharger compressors have a tip radius of 20 mm with shroud contour and blade profile tolerances of ± 100 μm [34]. With adequate scaling to the proposed microturbine rotor geometry with a compressor radius of 8 mm, the corresponding manufacturing tolerance is ± 40 μm. To contrast the physical samples with the ideal model topology, scans of the rotors have been conducted with an Artec Microstructured light 3D scanner of 23 μm spatial resolution and 10 μm point accuracy. Furthermore, CT scans were conducted with EasyTom S by RX solutions with 0.5 μm resolution. The results for the compressor and turbine surfaces are presented in Fig. 14 where dimensional deviations from the CAD model are labeled. Altogether, the scan results revealed significant differences between LCM and SLM-manufactured rotors in terms of surface finish, geometric accuracy, and printing artifacts. Both rotors present a reticulated structure on the blade surfaces, while layers in the z-direction are only visible at low horizontal slope surfaces. This is an artifact of the lateral resolution and the transverse layer height of the manufacturing processes, being (32 μm, 20 μm) and (50 μm, 30 μm) for LCM and SLM, respectively. Expectedly, the rotor produced by LCM technology demonstrates a smooth surface finish and high resemblance to the CAD geometry. Details such as the blade root radii (0.15 mm) are clearly resolved. In contrast, SLM rotor presents higher surface roughness, where artifacts such as prominent layer structure on the hub and stochastic grains give the impression of a fuzzy surface. Focusing on the compressor section, the blades of both parts are consistently thicker than the design geometry, with values of $\sim$110 μm and $\sim$40 μm for LCM and SLM, respectively. This value is likely associated with manufacturing resolution, limited by 35 μm sintering pixel resolution and 50 μm of laser spot size, respectively. Apart from the blade thickness offset, the blade surfaces are parallel to the model with deviations between ± 10 μm and ± 40 μm. Lastly, the tip diameter is in a tolerance field of ± 35 μm for both rotors.

On the turbine side, both processes show clear deficiencies at the blade shroud profile due to the overhung location. Since SLM and LCM use opposite printing directions, gravity effect is reversed resulting in corresponding deformation. In both processes, deviations as large as 200 μm can be observed. For future rotors, this effect will need to be considered during the design stage by compensating for the manufacturing deformation using a corrected 3D geometry for the blade profile.

When focusing on the smaller features of print, the ceramic SiAlON rotor produced with LCM shows very uniform surfaces absent any significant 3D printing artifacts. Therefore, the relative tolerances achieved with this process are similar to larger-scale casted parts except for the deviation in blade thickness. On the other hand, the Inconel 718 compressor rotor produced by SLM clearly presents higher deviations and greater number of printing artifacts. For example, in the vicinity of the shroud tip of the compressor inlet, a blunt thickening can be observed causing a blade height and thickness increase by up to 100 μm. This artifact has been repeatedly

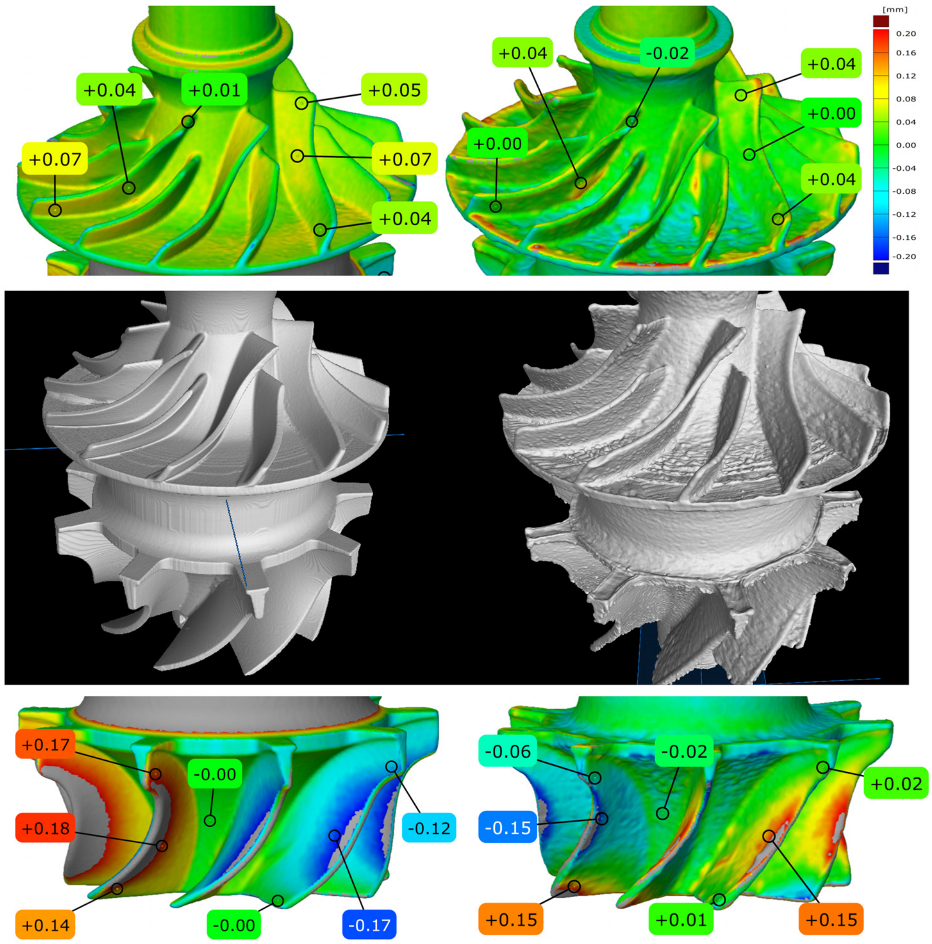

Fig. 14 Geometric deviations of compressor (top) and turbine (bottom) topologies between model and LCM produced SiAlON rotor (left) and SLM produced Inconel 718 rotor (right)

observed across multiple manufacturing batches, and it is expected to reduce compressor efficiency, as highest relative velocity occurs at this location. The aerodynamic implications are earlier shroud separation and increased local Mach numbers as compared to the smooth rotors.

In addition to geometrical inaccuracy, the LCM and SLM processes also result in different surface roughness profiles, which were measured on cut-open rotors using a tactile profilometer (MarSurf PS10, Mahr). As shown in Fig. 15, the Inconel rotor produced via SLM exhibits significantly higher surface roughness values than the SiAlON rotor produced with LCM, with roughness mean values of 11 μm and 2 μm, respectively. The SLM surface is also characterized by dimples and spikes with heights up to 60 μm. These deviations, which are relatively large compared to the compressor flow passage blade height, are expected to have a significant impact on aerodynamic performance.

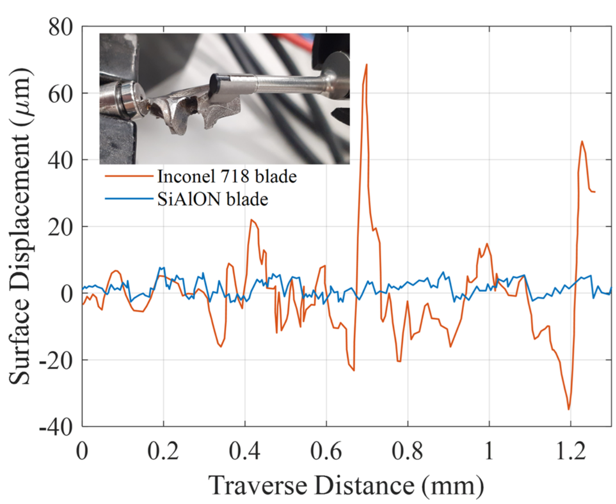

Fig. 15 Profilometer measurements along the surface of LCM produced SiAlON and SLM produced Inconel 718 rotors

Focusing on the internal structure resolved by the CT scan (Fig. 17), the SLM rotor images suggest that further optimization of print parameters is needed. The hatch structure is partially not connected to the outer shell, resulting in multiple cavities below the outer surface. The compressor leading edge has a significant impact on aerodynamic performance, and therefore should be physically represented to the highest possible fidelity—in this case best achieved by the LCM process, which accurately captures the elliptical leading-edge shape. The SLM leading edge is geometrically undefined with sharp spikes, which can result in flow separation at incidence. High surface roughness is observed on the compressor overhung slope at the internal cavity. The LCM rotor exhibits residuals of nonattached sintered material, which is likely a result of insufficient cleaning, as the internal cavity is difficult to access.

Furthermore, a porosity analysis was conducted to map the distribution of defect volume, as shown in Fig. 16. The Inconel 718 rotor revealed a large number of spherical-shaped cavities, which is a common occurrence in the SLM process and can be attributed to powder contaminations or process-induced trapped gas bubbles [6]. However, Inconel 718 exhibits ductile behavior, which allows it to

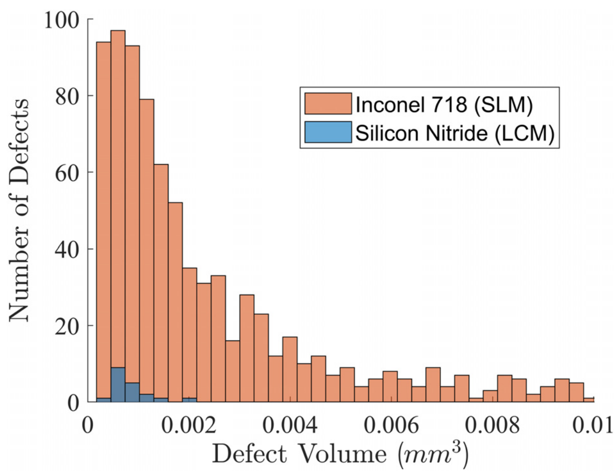

Fig. 16 Porosity defect volume distribution histogram for LCM produced SiAlON and SLM produced Inconel 718 rotors

compensate for stress concentrations. In comparison, SiAlON has low fracture toughness, making it more prone to failure due to stress concentrations at internal defects, and therefore requiring higher standards in terms of porosity. The CT scan showed that a few spherical cavities also exist in the SiAlON rotor, mostly at the outer radius of the compressor and turbine blade structures, in locations where relatively low stresses are expected.

Lastly, SEM micrographs were recorded to evaluate the microstructure of the processed SiAlON samples, as shown in Fig. 18. The surface of the LithaNit 780 sample appears as expected based on its composition, indicating that the material is of good quality and free of defects or irregularities. Further material analysis, including

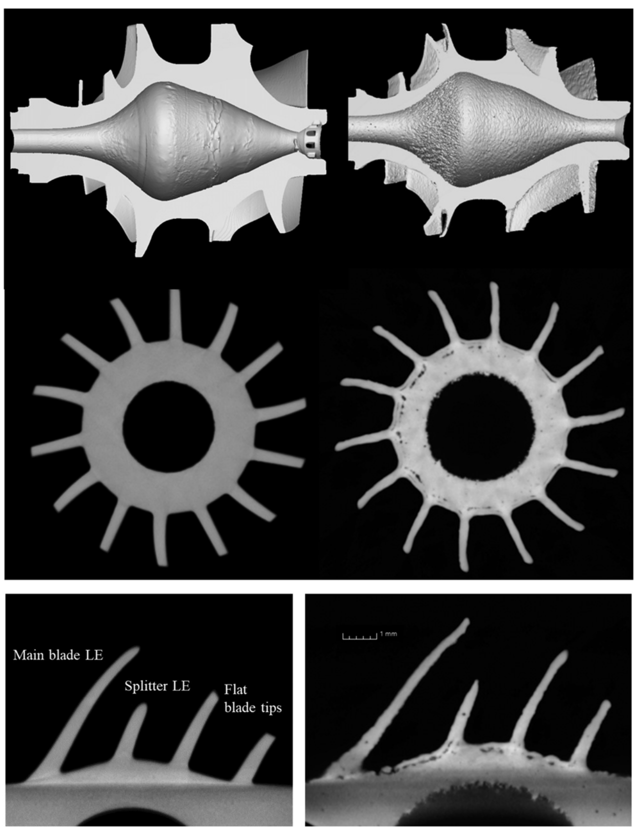

Fig. 17 CT scan of internal structure of LCM produced SiAlON rotor (left) and SLM produced Inconel 718 rotor (right), where bottom images are focused on the compressor leading edge

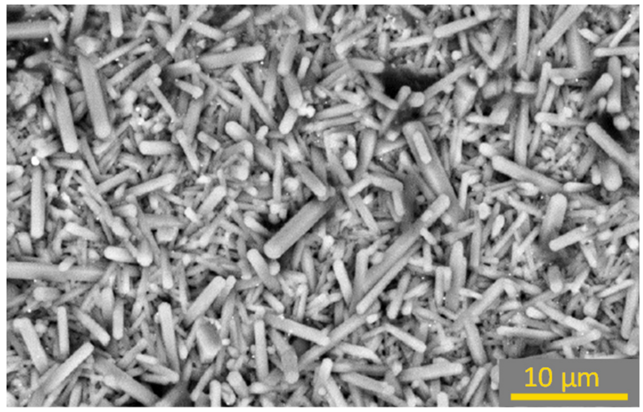

Fig. 18 SEM micrograph of a printed and sintered sample of LCM produced SiAlON (LithaNit 780)

analysis of fracture surface topology and X-ray diffraction, can be found in Ref. [22].

4.2 Aerodynamic Performance. In the following, three performance data sets are compared consisting of the experimental results for the LCM-manufactured SiAlON rotor and the SLM-manufactured Inconel 718 rotor as well as the CFD simulation results. The experiments and simulations were conducted at speeds up to 450,000 RPM. Experimental data was evaluated once steady-state conditions were reached. To protect the bearings, measurements were taken at a safe distance from the surge line. Figure 19 presents the compressor map at different speeds. The maximum measured pressure ratio is ~2.2 for 450,000 RPM, whereas the flowrate ranges from 1.2 g/s to 4.2 g/s. Depending on the operating point, Fig. 20 depicts the total-to-total polytropic efficiency of the rotors, which ranged from 60% to 85% depending on the operating point.

Comparing the experimental and CFD data pressure ratio (Fig. 19), simulation results exceed measured performance, while the SiAlON rotor continuously achieves a higher total pressure ratio than the Inconel rotor. The total rotor pressure is proportional to the tip velocity u_2, outlet blockage B_2, and relative flow angle β_2

$$P_{2t} \propto \eta_{\mathrm{ptt}} u_2^2 \left(1 - \frac{\dot{m}}{\rho_2 A_2 u_2} \frac{1}{1 - B_2} \tan(\beta_2)\right) \tag{11}$$

When comparing the experimental results between LCM and SLM processed rotors, it can be assumed that tip blockage and relative

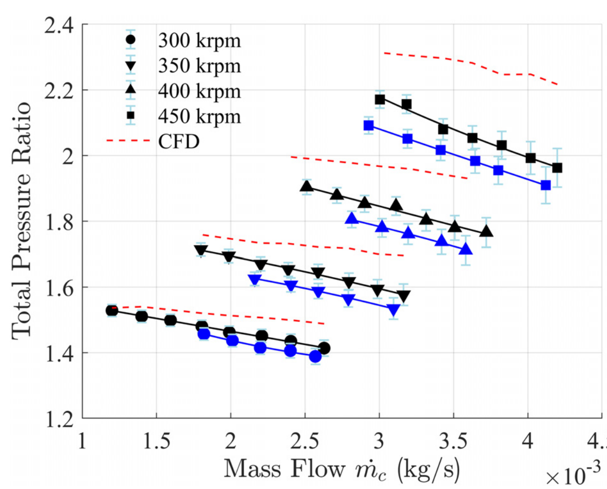

Fig. 19 Measured compressor pressure ratio for SiAlON rotor (black) and Inconel 718 rotor

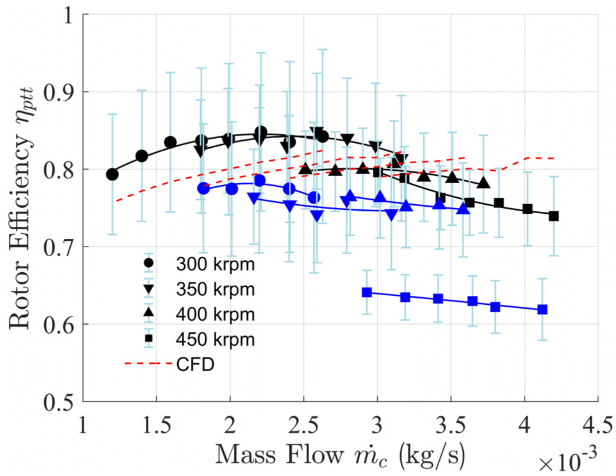

Fig. 20 Measured rotor efficiency for SiAlON rotor (black) and Inconel 718 rotor

flow angle do not deviate significantly. Therefore, the observed total pressure difference is caused by higher losses in the Inconel 718 compressor for the same turbine work input as the SiAlON rotor.

When comparing CFD results to experimental data, the outlet blockage may vary as it depends on the numeric prediction of flow separation inside the rotor. The measured data implies that flow separation is underpredicted by CFD, resulting in a lower outlet blockage and thus higher pressure ratio according to Eq. (11). Additionally, CFD simulations represent an idealized case with smooth, adiabatic walls which contributes to lower rotor losses and thus higher pressure ratio compared to experimental measurements. As depicted in Fig. 21, a large separation region is predicted at the rotor exit for a compressor flowrate of 4.2 g/s and rotational speed of 450,000 rpm. This indicates, that the selected relative velocity ratio from inlet to outlet (De-Haller number) of 0.4 was chosen too optimistic [35]. Owing to lower Reynolds numbers as compared to large-scale compressors, onset of separation occurs for smaller adverse pressure gradients, requiring a more conservative design of passage flow diffusion. These findings will be considered in the future for an updated microcompressor design.

The rotor total to total efficiency levels depicted in Fig. 20 shows that the CFD simulation results are mostly within the error bars of the measurements. At low flow rates, diabatic effects are more dominant and since the experiments were conducted in cold conditions, the rotor exit temperature drops, and measured efficiency is overpredicted compared to adiabatic CFD simulations. However, at higher flow rates the results become more reliable, suggesting that the SiAlON compressor efficiency falls below CFD predictions by up to 7%, which can be explained by idealized CFD geometry and surface conditions. The previously observed pressure ratio reduction from LCM to SLM process is also reflected in the rotor efficiency where the Inconel rotor performance is continuously lower than the SiAlON counterpart. This is in part owing to the geometrically undefined leading edge of the Inconel compressor, resulting in disproportional separation losses. Moreover, a particularly substantial efficiency decline is noted at the highest speed ~450,000 RPM, which is a likely ramification of higher roughness and printing artifacts (like dimples) on the Inconel 718 surface causing higher friction loss coefficient (c_f). For high rotational speeds and associated augmented relative frame velocity w, the pressure losses are expected to scale quadratically, as $\Delta P_{t,\text{friction}} \propto c_f w^2$, and dominate over other entropy generation mechanisms. To improve performance, electropolishing or grinding of the flow passage and rounding of the leading edge will be performed in the future.

5 Summary and Conclusion

The present study focuses on an in-depth depiction of the design, production, assembly, and high-speed testing of monolithic rotors produced by Lithography-based ceramic manufacturing and selective laser melting. This is the first time that microturbomachinery components made using these methods have been directly compared using a set of aerodynamic and manufacturing quality assurance diagnostics. The aerodynamic implications of support-free compressor and turbine design were examined, and the manufacturing considerations and process parameters for both processes were formulated in detail. Quality analysis of the parts, conducted via surface and CT scans, as well as SEM micrography, revealed that the LCM rotors had higher geometric detail, better surface finish, less manufacturing-related surface artifacts, and lower porosity compared to the SLM rotors. In the following, a dedicated rotor test facility was developed and used to compare the aerodynamic performance of metallic and ceramic compressors as well as CFD simulations at speeds of up to 450,000 RPM, resulting in a measured rotor pressure ratio of up to 2.2 for flow rates between 1.2 g/s and 4.2 g/s. Moreover, the aerodynamic findings indicated that 3D printed microturbomachinery can achieve relatively high compressor rotor efficiency of up to 80%. The tests also revealed that the SiAlON parts fabricated via LCM process exhibited superior aerodynamic performance, improved pressure ratio, and efficiency compared to the SLM-produced Inconel 718 compressors due to the latter's higher surface roughness and geometric deficiencies. This

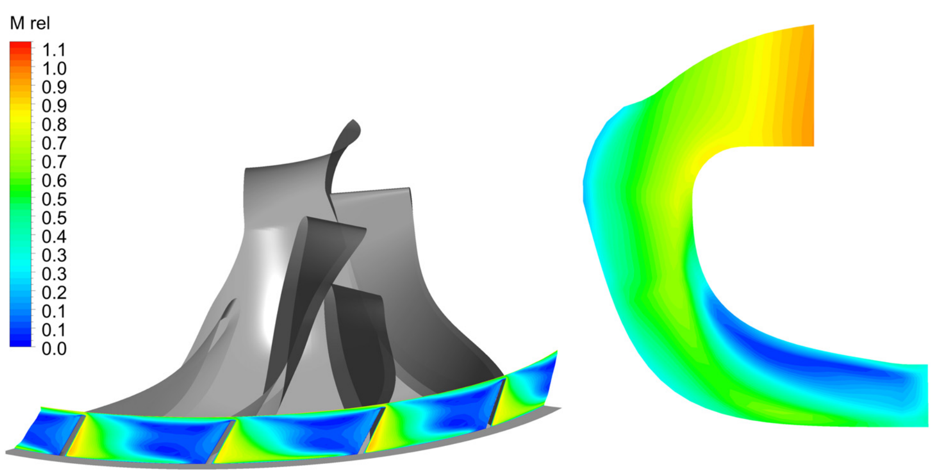

Fig. 21 Relative Mach numbers at rotor exit (left) and averaged in the meridional plane (right), indicating a large separation region

observation holds a promise for LCM technology to be particularly useful in turbomachinery applications where compact size and high efficiency are important, such as air conditioning systems, refrigeration units, heat pumps, and medical devices. In the future, long-term testing under hot conditions, structural integrity tests, and statistical failure analysis need to be conducted to qualify the rotor manufacturing approach for high service performance demands.

Acknowledgment

The present research was supported by U.S. Army Research Laboratory under Cooperative Agreement No. W911NF-22-2-0192. The views and conclusions contained in this document are those of the authors and should not be interpreted as representing the official policies, either expressed or implied, of the Army Research Laboratory or the U.S. Government. The U.S. Government is authorized to reproduce and distribute reprints for Government purposes notwithstanding any copyright notation herein.

Funding Data

- Minerva Research Center (Grant No. AZ5746940764; Funder ID: 10.13039/501100001658).
- The Crown Vanguard Award for Science and Technology Fund, along with Technion Additive Manufacturing Center, Equipment (Grant No. CFP-2021; Funder ID: 10.13039/100006754).
- Peter Munk Research Institute, Center for Security Science and Technology (Funder ID: 10.13039/100006754).
- U.S. Army Research Laboratory (Funder ID: 10.13039/100006754).

Data Availability Statement

The datasets generated and supporting the findings of this article are obtainable from the corresponding author upon reasonable request.

References

[1] Badum, L., Leizeronok, B., and Cukurel, B., 2021, "New Insights From Conceptual Design of an Additive Manufactured 300W Micro Gas Turbine Towards UAV Applications," ASME J. Eng. Gas Turbines Power, **143**(2), p. 021006.

[2] Isomura, K., Teramoto, S., Togo, S.-I., Hikichi, K., Endo, Y., and Tanaka, S., 2006, "Effects of Reynolds Number and Tip Clearances on the Performance of a Centrifugal Compressor at Micro Scale," ASME Paper No. GT2006-90637.

[3] Verstraete, T., Alsalihi, Z., and van den Braembussche, R. A., 2010, "Multidisciplinary Optimization of a Radial Compressor for Microgas Turbine Applications," ASME J. Turbomach., **132**(3), p. 31004.

[4] Klocke, F., Klink, A., Veselovac, D., Aspinwall, D. K., Soo, S. L., Schmidt, M., Schilp, J., Levy, G., and Kruth, J.-P., 2014, "Turbomachinery Component Manufacture by Application of Electrochemical, Electro-Physical and Photonic Processes," CIRP Ann., **63**(2), pp. 703–726.

[5] Zhang, Y., Duda, T., Scobie, J. A., Sangan, C., Copeland, C. D., and Redwood, A., 2018, "Design of an Air-Cooled Radial Turbine: Part 1—Computational Modelling," ASME Paper No. GT2018-76378.

[6] Wang, X., Gong, X., and Chou, K., 2017, "Review on Powder-Bed Laser Additive Manufacturing of Inconel 718 Parts," Proc. Inst. Mech. Eng., Part B: J. Eng. Manuf., **231**(11), pp. 1890–1903.

[7] Kaya, H., 1999, "The Application of Ceramic-Matrix Composites to the Automotive Ceramic Gas Turbine," Compos. Sci. Technol., **59**(6), pp. 861–872.

[8] McLEAN, A. F., 1970, "The Application of Ceramics to the Small Gas Turbine," ASME Paper No. 70-GT-105.

[9] DeBell, G. C., and Secord, J. R., 1981, "Development and Testing of a Ceramic Turbocharger Rotor," ASME Paper No. 81-GT-195.

[10] Am El-Amir, A., El-Maddah, A. A., Ewais, E. M. M., El-Sheikh, S. M., Bayoumi, I. M. I., and Ahmed, Y. M., 2021, "Sialon From Synthesis to Applications: An Overview," J. Asian Ceram. Soc., **9**(4), pp. 1390–1418.

[11] Layden, G. K., 1977, "Pressureless Sintering of SiAlON Gas Turbine Components," United Technologies Research Center East Hartford Conn, East Hartfort, CT, Report No. US Navy Report NADC-75207-30.

[12] Kang, S., 2002, "Fabrication of Functional Mesoscopic Ceramic Parts for Micro Gas Turbine Engines," Dissertation, Stanford University, Stanford, CA.

[13] Kang, S., Johnston, J. P., Arima, T., Matsunaga, M., Tsuru, H., and Printz, F. B., 2004, "Microscale Radial-Flow Compressor Impeller Made of Silicon Nitride: Manufacturing and Performance," ASME J. Eng. Gas Turbines Power, **126**(2), pp. 358–365.

[14] Liu, H. C., Kang, S., Prinz, F. B., and Stampfl, J., 2002, "Fabrication of Ceramic Components for Micro Gas Turbine Engines," 26th Annual Conference on Composites, Advanced Ceramics, Materials, and Structures: B, the American Ceramic Society, New York, Dec., pp. 43–50.

[15] Zwyssig, C., 2008, "An Ultra-High-Speed Electrical Drive System," Dissertation, ETH Zurich, Zürich, Switzerland.

[16] Markovic, M., and Perriard, Y., 2006, "Simplified Design Methodology for a Slotless Brushless DC Motor," IEEE Trans. Magnetics, **42**(12), pp. 3842–3846.

[17] Pfister, P.-D., and Perriard, Y., 2010, "Very-High-Speed Slotless Permanent-Magnet Motors: Analytical Modeling, Optimization, Design, and Torque Measurement Methods," IEEE Trans. Ind. Electron., **57**(1), pp. 296–303.

[18] Cukurel, B., 2021, "Ultra-Micro Gas Turbine Generator," Patent No. WO2021144791A1.

[19] Steinbach, AG, 2023, "Design Guide," Steinbach AG, Detmold, Germany, accessed Sept. 22, 2023, https://www.steinbach-ag.de/en/technical-ceramics/know-how/design-guide.html

[20] Rusch, D., and Casey, M., 2013, "The Design Space Boundaries for High Flow Capacity Centrifugal Compressors," ASME J. Turbomach., **135**(3), p. 31035.

[21] Whitfield, A., 1990, "The Preliminary Design of Radial Inflow Turbines," ASME J. Turbomach., **112**(1), pp. 50–57.

[22] Altun, A. A., Prochaska, T., Konegger, T., and Schwentenwein, M., 2020, "Dense, Strong, and Precise Silicon Nitride-Based Ceramic Parts by Lithography-Based Ceramic Manufacturing," Appl. Sci., **10**(3), p. 996.

[23] Mitteramskogler, G., Gmeiner, R., Felzmann, R., Gruber, S., Hofstetter, C., Stampfl, J., Ebert, J., Wachter, W., and Laubersheimer, J., 2014, "Light Curing Strategies for Lithography-Based Additive Manufacturing of Customized Ceramics," Addit. Manuf., **1–4**, pp. 110–118.

[24] Schwentenwein, M., and Homa, J., 2015, "Additive Manufacturing of Dense Alumina Ceramics," Int. J. Appl. Ceram. Technol., **12**(1), pp. 1–7.

[25] Laakso, P., Riipinen, T., Laukkanen, A., Andersson, T., Jokinen, A., Revuelta, A., and Ruusuvuori, K., 2016, "Optimization and Simulation of SLM Process for High Density H13 Tool Steel Parts," Phys. Procedia, **83**, pp. 26–35.

[26] ISO 21940-11, 2005, "Mechanical Vibration–Rotor Balancing Part 11: Verfahren Und Toleranzen for Rotoren Mit Starrem Verhalten," British Standards and International Standards Organisation, London, UK.

[27] Casey, M., and Robinson, C., 2021, *Radial Flow Turbocompressors*, Cambridge University Press, Cambridge, UK.

[28] Fernelius, M., and Gorrell, S., 2014, "Thermocouple Recovery Factor for Temperature Measurements in Turbomachinery Test Facilities," AIAA Paper No. 2014–0791.

[29] B. S. ISO, 2005, "5168: 2005 Measurement of Fluid Flow–Procedures for the Evaluation of Uncertainties," British Standards Int. Standards Organisation, London, UK.

[30] Kennedy, I., Chen, Z., Ceen, B., Jones, S., and Copeland, C. D., 2019, "Experimental Investigation of an Inverted Brayton Cycle for Exhaust Gas Energy Recovery," ASME J. Eng. Gas Turbines Power, **141**(3), p. 032301.

[31] Aungier, R. H., 2000, *Centrifugal Compressors*, ASME Press, New York.

[32] Gibson, L., Galloway, L., Kim, S. I., and Spence, S., 2017, "Assessment of Turbulence Model Predictions for a Centrifugal Compressor Simulation," J. Glob. Power Propuls. Soc., **1**, pp. 2I1890–156.

[33] Salviano, L. O., Gasparin, E. E., Mattos, V. C. N., Barbizan, B., Saltara, F., de Mello, P. E. B., Dezan, D. J., and Yanagihara, J. I., 2021, "Sensitivity Analysis and Optimization of a CO2 Centrifugal Compressor Impeller With a Vaneless Diffuser," Struct. Multidiscip. Optim., **64**(3), pp. 1607–1627.

[34] Javed, A., Pecnik, R., Olivero, M., and van Buijtenen, J. P., 2012, "Effects of Manufacturing Noise on Microturbine Centrifugal Impeller Performance," ASME J. Eng. Gas Turbines Power, **134**(10), p. 103202.

[35] Came, P. M., and Robinson, C. J., 1998, "Centrifugal Compressor Design," Proc. Inst. Mech. Eng., Part C: J. Mech. Eng. Sci., **213**(2), pp. 139–155.